Non-paraxial contributions to the far-field pattern of surface-emitting lasers: a manifestation of the momentum-space wavefunctions of quantum billiards

2011 J. Opt. 13 075705

(http://iopscience.iop.org/2040-8986/13/7/075705)

IOP Publishing Journal of Optics
J. Opt. **13** (2011) 075705 (7pp) doi:10.1088/2040-8978/13/7/075705

Non-paraxial contributions to the far-field pattern of surface-emitting lasers: a manifestation of the momentum-space wavefunctions of quantum billiards

Y T Yu, Y J Huang, P Y Chiang, Y C Lin, K F Huang and Y F Chen[1]

Department of Electrophysics, National Chiao Tung University, Hsinchu, Taiwan

E-mail: yfchen@cc.nctu.edu.tw

Received 5 January 2011, accepted for publication 19 April 2011
Published 12 May 2011
Online at stacks.iop.org/JOpt/13/075705

Abstract
We investigated experimentally non-paraxial contributions to the high-order far-field pattern of large-area vertical-cavity surface-emitting lasers in order to explore by analogy the momentum-space wave distributions of quantum billiards. Our results reveal that non-paraxial contributions significantly influence the morphology of the high-order far-field pattern. A fast reliable method is developed for transforming the experimental far-field patterns to the correct Fourier transform of the corresponding near-field lasing modes. In this way we visualize the momentum-space (p–q) wavefunctions of quantum billiards.

Keywords: surface-emitting laser, non-paraxial effect, far-field pattern, quantum billiards

(Some figures in this article are in colour only in the electronic version)

1. Introduction

The vertical-cavity surface-emitting laser (VCSEL) has been identified as a promising light source for applications in short distance communication, data transmission, and sensors [1, 2]. There has been intensive research on physical properties of the VCSEL, including the optical feedback dynamics, polarization, and transverse pattern formation [3–6]. Recently, the analogy between the Helmholtz equation and the time-independent Schrödinger equation has enables us to exploit the transverse near-field patterns of oxide-confined VCSELs to visualize the coordinate-space wavefunctions of 2D quantum billiards with the same lateral shapes [7–10]. Quantum billiard systems have been widely used to explore many striking mesoscopic phenomena such as electron transport [11], conductance fluctuations in quantum dots [12, 13], and the diffraction in time effect [14].

Since the far-field pattern is the Fourier transform of the near-field pattern based on the paraxial approximation, the momentum-space wavefunctions of 2D quantum billiards can also be analogously observed with the high-order lasing modes of VCSELs [8]. Generation of the higher-order transverse modes can provide more interesting perspectives for the exploration of the quantum–classical connection. However, during the free-space propagation of the higher-order lasing modes, non-paraxial contributions to the total wavevector k may significantly influence the far-field patterns. Therefore, it is essentially important to develop an appropriate correcting method for extracting the momentum-space wavefunctions from the experimental far-field patterns with the substantial non-paraxial contribution.

In this work, we first exploit square-shape large-aperture VCSELs to experimentally investigate the difference between the low-order and high-order far-field transverse patterns. Experimental results reveal that the high-order far-field patterns display significant bowing toward the center of the device. We define this effect as the pincushion curving of the Fourier transform of the near-field wavefunction and we refer to it as pincushion curving. We employ the stationary phase

[1] Address for correspondence: Department of Electrophysics, National Chiao Tung University, 1001 Ta Hsueh Road, Hsinchu 30050, Taiwan.

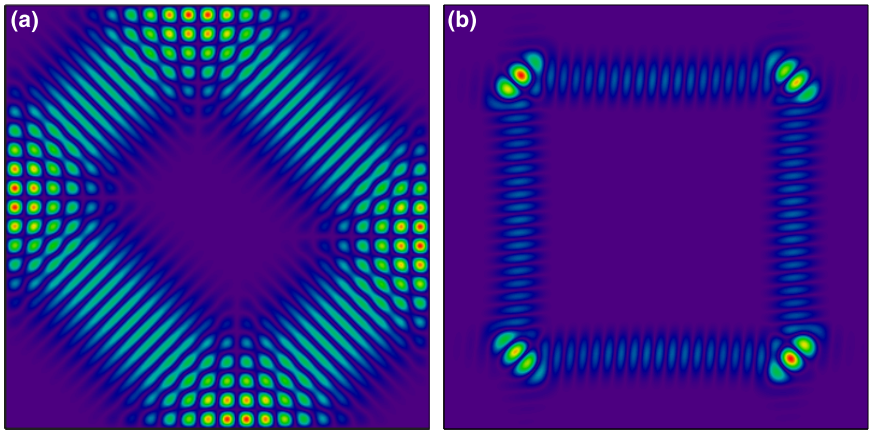

Figure 1. (a) Theoretically calculated coherent state $|S^{1,1,0.55\pi}_{22,5,+}(x, y)|^2$ in a 2D square billiard; (b) the correspondence momentum space.

method [15] to confirm that the curving feature arises from the non-paraxial contribution. Moreover, a useful mapping is developed to recover the momentum-space wave patterns of 2D quantum billiards from the experimental far-field lasing patterns. We further numerically explore the higher-order eigenstates of equilateral triangular VCSELs to demonstrate that the pincushion curving is a typical feature of the non-paraxial contribution to the far-field patterns.

From the viewpoint of experimental measurements, the motivation and significance of this research as well as relevant materials can be more clearly appreciated. The observation of near-field patterns of lasing modes inevitably requires a re-imaging optics with sufficiently high numerical aperture, whereas the far-field patterns can be directly measured without any re-imaging optics by simply using a screen. It is well known that the far-field pattern can be numerically obtained from the experimental near-field patterns with the diffraction theory. However, under the circumstances of a strong non-paraxial contribution, it is scientifically important to extract the information of the near-field pattern from the experimental far-field pattern. Our work is aimed at developing a straightforward procedure for mapping the experimental far-field lasing pattern into the accurate Fourier transform pattern of the near-field mode.

2. Coherent states in square quantum billiards

To begin with, we give a brief synopsis for the coordinate-space and momentum-space representations of the coherent states in a square billiard. The choice of the square-shape geometry is motivated by a recent experiment where the wavefunctions localized on classical periodic orbits were found not only to be the persistent states in open square quantum dots but also to be associated with the striking phenomena of conductance fluctuations [12, 13]. For a square billiard with the vertices at $(\pm a/2, \pm a/2)$ and $(\pm a/2, \mp a/2)$, the quantum eigenstates $\psi_{\tilde{m},\tilde{n}}(x, y)$ are given by [16]

$$\psi_{\tilde{m},\tilde{n}}(x, y) = (2/a)\sin\left[k_{\tilde{m}}\,(x + a/2)\right]\sin\left[k_{\tilde{n}}\,(y + a/2)\right], \tag{1}$$

where $k_n = n\pi/a$ $(n = 1, 2, 3, \ldots)$ and a is the length of the square boundary. On the other hand, each family of classical periodic orbits in a square billiard can be denoted by with three parameters (p, q, ϕ), where p and q are two positive integers describing the number of collisions with horizontal and vertical walls, and the phase factor ϕ is in the range of $-\pi$ to π that is related to the wall positions of specular reflection points [16]. It has been verified that with the Schwinger SU(2) representation the coherent states associated with periodic orbits (p, q, ϕ) can be analytically expressed as [16]

$$\Psi^{p,q,\phi}_{N,M}(x, y) = \sum_{K=-M}^{M} C_{M,K}\,\mathrm{e}^{\mathrm{i}K\phi}\psi_{qN+pK,pN-qK}(x, y), \tag{2}$$

where N represents the order of the coherent state, $C_{M,K} = \frac{1}{2^M}\binom{2M}{M+K}^{1/2}$ is the weighting coefficient, and $\binom{n}{k} = \frac{n!}{k!(n-k)!}$ represents the binomial coefficient. Note that the coherent states obtained as a linear superposition of a few nearly degenerate eigenstates have been verified to be the persistent stationary states in real mesoscopic systems and to display quantum interference features in the classical periodic orbits.

With the Fourier transform, the momentum-space representation of the coherent states $\Psi^{p,q,\phi}_{N,M}(x, y)$ is given by

$$\begin{aligned}\tilde{\Psi}^{p,q,\phi}_{N,M}(k_x, k_y) = &\sum_{K=-M}^{M} C_{M,K}\,\mathrm{e}^{\mathrm{i}K\phi}\\ &\times\{[F(k_x; k_{qN+pK}, a) - F(k_x; -k_{qN+pK}, a)]\\ &\times[F(k_y; k_{pN-qK}, a) - F(k_y; -k_{qN+pK}, a)]\}\end{aligned} \tag{3}$$

with

$$F(k_i; k_n, a) = \mathrm{e}^{\frac{\mathrm{i}k_n a}{2}}\frac{\sin[(k_i + k_n)\,a/2]}{(k_i + k_n)}, \tag{4}$$

where k_i $(i = x, y)$ are the wavevectors in the x-direction and y-direction, respectively. Note that the coherent states $\Psi^{p,q,\phi}_{N,M}(x, y)$ behave as traveling waves in the transverse plane. The standing-wave representation is given by $S^{p,q,\phi}_{N,M,\pm}(x, y) = [\Psi^{p,q,\phi}_{N,M}(x, y) \pm \Psi^{p,q,-\phi}_{N,M}(x, y)]/\sqrt{2}$. Consequently, the momentum-space representation of the coherent states $S^{p,q,\pm\phi}_{N,M}(x, y)$ is given by $\tilde{S}^{p,q,\phi}_{N,M,\pm}(k_x, k_y) = [\tilde{\Psi}^{p,q,\phi}_{N,M}(k_x, k_y) \pm \tilde{\Psi}^{p,q,-\phi}_{N,M}(k_x, k_y)]/\sqrt{2}$. Figures 1(a) and (b)

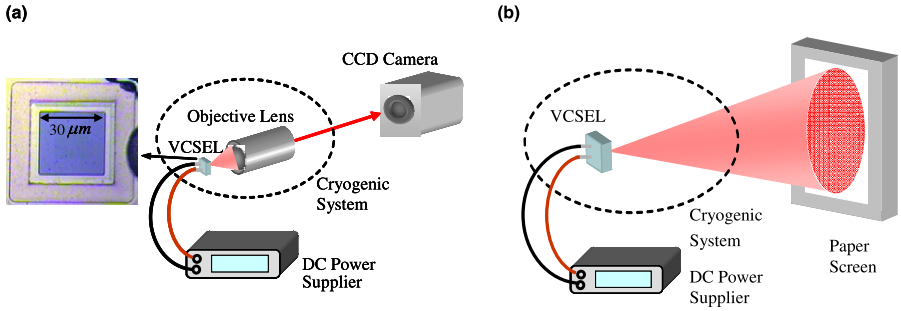

Figure 2. Schematics of the VCSEL device structure and the experimental setup: (a) measurement of the near-field pattern and (b) measurement of the far-field pattern.

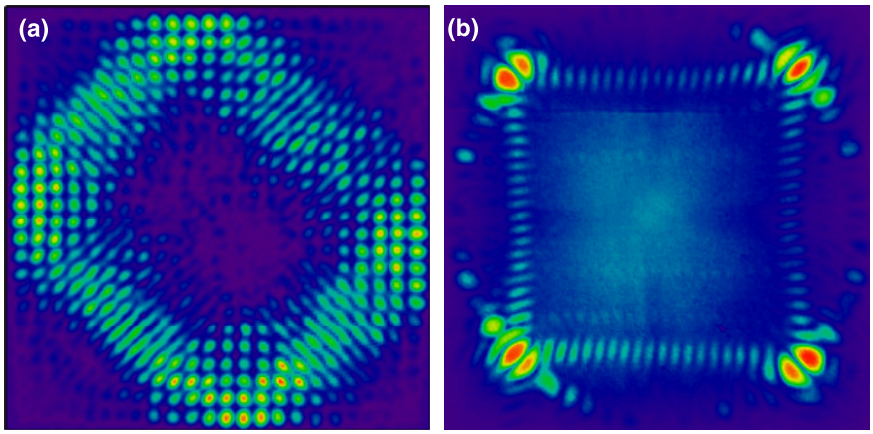

Figure 3. Experimental patterns of a square-shape VCSEL obtained with the detuning of $\Delta\omega/2\pi = 2.7$ THz: (a) near-field pattern; (b) far-field pattern.

illustrate the numerical patterns for the coordinate-space wave patterns $|S^{p,q,\phi}_{N,M,+}(x, y)|^2$ and the momentum-space wave patterns $|\tilde{S}^{p,q,\phi}_{N,M,+}(k_x, k_y)|^2$, respectively, with the parameters $(p, q) = (1, 1)$, $(N, M) = (22, 5)$, and $\phi = 0.55\pi$. It can be seen that the real-space wave pattern is concentrated along a diamond-shaped classical trajectory in the transverse plane $(x–y)$ and the corresponding momentum-space wavefunction exhibits high-intensity lobes at the corners of the aperture with flower-like structure and relatively weak stripes connecting them.

3. Experimental results

For VCSELs, the transverse order of the lasing mode depends on the frequency detuning $\Delta\omega = \omega - \omega_c$, where ω is the emission angular frequency and ω_c is the longitudinal cavity resonance. Experimentally, we fabricated several large-aperture square-shape VCSELs with different frequency detunings to explore the far-field transverse patterns of higher-order modes. Figure 2 depicts a top view of the VCSEL to show the square aperture and the experimental setup for near-field (figure 2(a)) and far-field (figure 2(b)) measurements. The size of the oxide aperture was 30×30 μm^2 and the emission wavelength was designed to be around 800 nm. The device structures of the oxide-confined VCSELs were similar to those described by [6]. The VCSELs were placed in a cryogenic system with a temperature stability of 0.1 K in the range of 80–300 K. A power supply providing current with a precision of 0.01 mA was utilized to drive the VCSEL. The near-field patterns were measured by a charge-coupled device (CCD) camera (Coherent, Beam-Code) with an objective lens (Mitsutoyo, numerical aperture 0.9). The far-field pattern was measured using a digital camera by directly projecting the laser beam on a scattering paper screen at a distance about 20–30 cm away from the VCSEL.

Figure 3 shows the near-field pattern and the corresponding far-field pattern for the experimental lasing mode obtained with the detuning of $\Delta\omega/2\pi = 2.7$ THz. It can be seen that the experimental patterns agree very well with the numerical results shown in figure 1 for the coordinate-space and momentum-space wavefunctions of a square quantum billiard. Next we generated a higher-order coherent state with a larger detuning. Figure 4 shows the experimental near-field pattern and the corresponding far-field pattern of the lasing mode obtained with the detuning of $\Delta\omega/2\pi = 6.9$ THz. The morphology of the near-field pattern (figure 4(a)) can be found to be in good agreement with the theoretical result; however, the far field (figure 4(b)) displays a significant pincushion curving when compared with a mode of lower transverse order (figure 3(b)). Experimental results reveal that the pincushion curving in the far-field distribution is independent of the pumping current in the range of 1.0–1.5 times the threshold

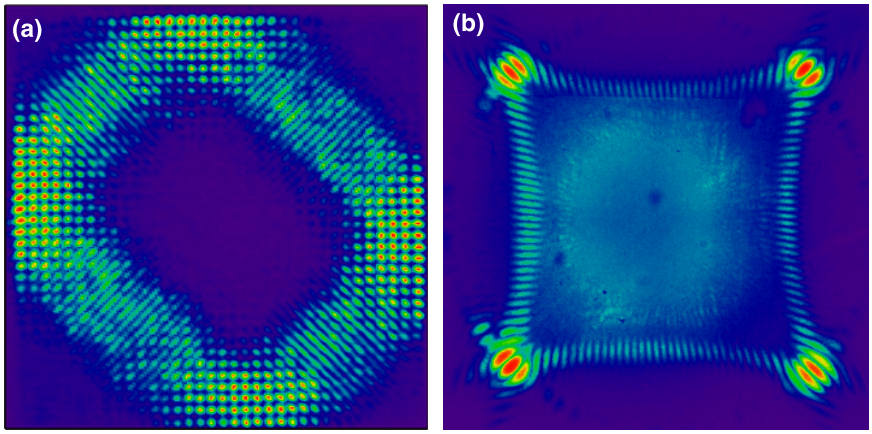

Figure 4. Experimental patterns of a square-shape VCSEL obtained with the detuning of $\Delta\omega/2\pi = 6.9$ THz: (a) near-field pattern; (b) far-field pattern.

level. Furthermore, the optical spectra indicate that the gray area in the central part of the far-field patterns in figures 3 and 4 arises from the amplified spontaneous emission. Consequently, the thermal lensing effect can be confirmed to be not the major mechanism in the formation of the pincushion curving. The origin of the present pincushion curving comes from the non-paraxial contribution because the transverse wavevector k_t is no longer much smaller than the longitudinal wavevector k_z for very high-order modes of VCSELs. Therefore, the non-paraxial contribution needs to be considered to obtain an accurate correspondence between the far-field pattern of high-order lasing modes of VCSELs and the momentum-space wavefunctions of quantum billiards. In section 4 we exploit the stationary phase method [15] to analyze the non-paraxial contribution and to develop a fast procedure for recovering the momentum-space wave patterns from the far-field patterns of high-order lasing modes of VCSELs.

4. Theoretical analysis and the recovery method

The propagation of a monochromatic near-field distribution $u_0(x, y)$ at $z = 0$ can be described in terms of a superposition of plane waves [17]:

$$u(x, y, z) = \int_{-\infty}^{\infty} \mathrm{d}k_x \int_{-\infty}^{\infty} \mathrm{d}k_y \, \tilde{u}_0(k_x, k_y) \mathrm{e}^{\mathrm{i}(k_x x + k_y y + k_z z)}, \quad (5)$$

where $k_z = \sqrt{k^2 - k_x^2 - k_y^2}$, and $\tilde{u}_0(k_x, k_y)$ is the Fourier transform of the near-field distribution $u_0(x, y)$. When the Fraunhofer approximation is valid, the far-field distribution with $kz \to \infty$ can be shown to be [17]

$$u(x, y, z) = \frac{2\pi k}{\mathrm{i}z} \mathrm{e}^{\mathrm{i}[k(x^2+y^2)/(2z)]} \mathrm{e}^{\mathrm{i}kz} \tilde{u}_0\left(k\frac{x}{z}, k\frac{y}{z}\right). \quad (6)$$

Equation (6) indicates that the far-field pattern $|u(x, y, z)|$ is related to the Fourier transform pattern of the near-field distribution $|\tilde{u}_0(k_x, k_y)|$ with the arguments of $k_x = kx/z$ and $k_y = ky/z$. When the non-paraxial contribution is significant, the stationary phase method [15, 18–20] is usually employed to derive the far-field distribution and this results in

$$u(x, y, z) = \frac{2\pi k z}{\mathrm{i}r^2} \mathrm{e}^{\mathrm{i}kr} \tilde{u}_0\left(k\frac{x}{r}, k\frac{y}{r}\right), \quad (7)$$

where $r = \sqrt{x^2 + y^2 + z^2}$. As a consequence, the accurate relationship between the far-field distribution and the Fourier transform of the near-field distribution is given by equation (7) instead of equation (6).

We used equations (2) and (7) to calculate the near-field and far-field VCSEL patterns and to show the analogy between them and the trajectories of the coherent states of square billiards with different orders N. Figure 5 shows the calculated results for the near-field patterns $|S^{p,q,\phi}_{N,M,+}(x, y)|^2$ with different orders of $N = 20$, 30, and 40 (figures 5(a)–(c)) and the corresponding far-field patterns (figures 5(a′)–(c′)). The values of the parameters used in the calculation are $(p, q) = (1, 1)$, $M = 5$, and $\phi = 0.55\pi$. It can be seen that the influence of the non-paraxial contribution leads to the pincushion curving in the far-field pattern with respect to the Fourier transform of the near-field distribution. The higher the transverse order is, the more curved the far-field pattern becomes. This result enables us to confirm the origin of the experimental patterns shown in figure 4. Since the far-field patterns of the VCSEL's lasing modes can be straightforwardly observed, it is practically useful to develop a transform procedure for recovering the momentum-space wave patterns from the experimental far-field patterns.

Equation (7) reveals that the far-field pattern $|u(x, y, z)|$ beyond the paraxial approximation is related to the Fourier transform pattern of the near-field distribution $|\tilde{u}_0(k_x, k_y)|$ with the arguments of $k_x = kx/r$ and $k_y = ky/r$. In other words, the experimental far-field pattern $|u(x, y, z)|$ can be used to obtain the Fourier transform pattern of the near-field distribution $|\tilde{u}_0(k_x, k_y)|$ via the change of the arguments of $x = k_x r/k$ and $y = k_y r/k$. However, since the variable r is a function of the variables x and y, the expressions $x = k_x r/k$ and $y = k_y r/k$ cannot be applied directly. For solving this problem, we use the asymptotic property of the free-space propagation to obtain the identity $r/k = z/k_z =$

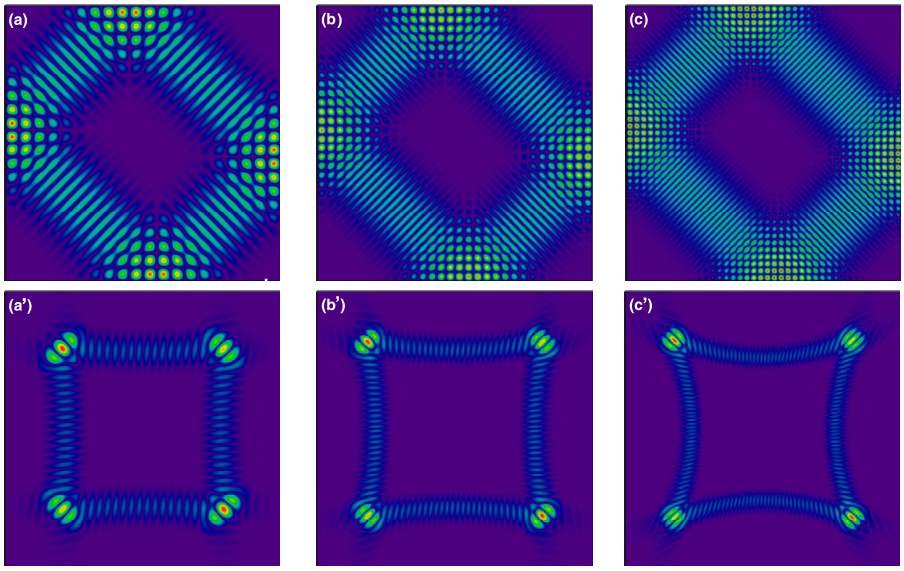

Figure 5. Numerically calculated near-field patterns of resonance modes with transverse order: (a) $N = 20$, (b) $N = 30$, (c) $N = 40$, and ((a′)–(c′)) the corresponding far-field patterns obtained by using the stationary phase method.

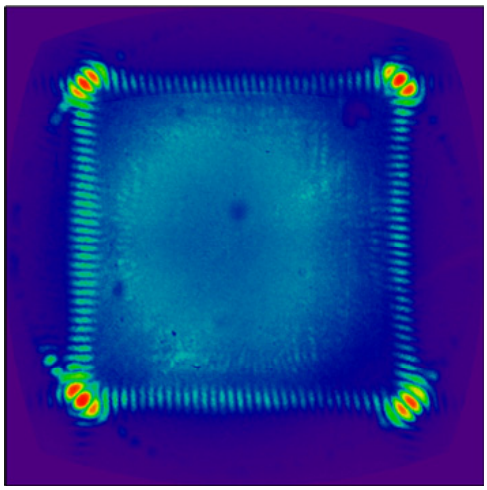

Figure 6. Reconstructed pattern for the far-field pattern shown in figure 4(b), to correspond to the Fourier transform pattern of the near-field distribution shown in figure 4(a).

$z/\sqrt{k^2 - k_x^2 - k_y^2}$. With this identity, the expressions $x = k_x r/k$ and $y = k_y r/k$ can be given as

$$x = k_x z \Big/ \sqrt{k^2 - k_x^2 - k_y^2} \tag{8}$$

and

$$y = k_y z \Big/ \sqrt{k^2 - k_x^2 - k_y^2}. \tag{9}$$

As a result, the Fourier transform pattern of the near-field distribution $|\tilde{u}_0(k_x, k_y)|$ can be straightforwardly obtained from the experimental far-field pattern $|u(x, y, z)|$ with the change of the arguments as in equations (8) and (9). Note that the far-field distribution intrinsically represents an angular field distribution that is essentially independent of the distance from the source. Equations (8) and (9) clearly reveal that the relationship between the transverse momentum (k_x, k_y) and the screen position (x, y) for recording the experimental far-field amplitude is not a linear mapping. It can be easily found that only when the non-paraxial contribution is negligible, i.e. $k^2 \gg k_{x,y}^2$, can the screen position (x, y) be linearly mapped to the specific transverse momentum (k_x, k_y). To the best of our knowledge, this is the first time that a useful mapping has been developed for obtaining the Fourier transform pattern of a near-field distribution from a corresponding far-field pattern that is subject to the influence of a non-paraxial contribution.

Applying the arguments of equations (8) and (9) to the experimental result shown in figure 4(b), the accurate Fourier transform pattern of the near-field distribution shown in figure 4(a) can be numerically reconstructed and it is depicted in figure 6. It can be seen that the pincushion curving of the original far-field pattern is almost completely eliminated. The morphology of the reconstructed pattern agrees very well with the momentum-space distribution of the coherent state shown in figure 1(b) with the transverse order of $N = 36$. In order to analyze quantitatively the correlation of these patterns, we calculate the spatial correlation function which is given by

$$g\,(\vec{\tau}) = \langle f_1\,(\vec{r} + \vec{\tau})\; f_2\,(\vec{r})\rangle\,, \tag{10}$$

where $f_1(\vec{r} + \vec{\tau})$ and $f_2(\vec{r})$ are normalized functions with the variable of position. Two functions are highly related to each other when $g(\vec{\tau})$ approaches the value of 1. Substituting the normalized reconstructed wave pattern and the momentum-space distribution of the coherent state with the transverse order of $N = 36$ into equation (8), we can obtain the value of 0.837. The calculated result reveals that the two patterns are highly correlated.

In addition to square billiards, the equilateral triangular structure is a classically non-separable but integrable system which also plays an important role in quantum billiards. Recently, various high-order modes of equilateral triangular

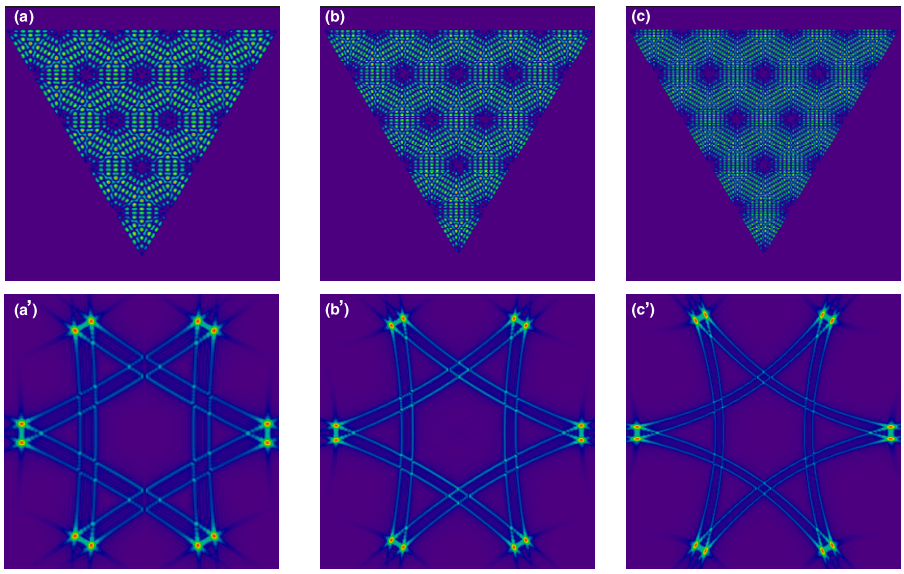

Figure 7. Numerically calculated wave patterns of eigenstates of an equilateral triangular VCSEL with transverse order: (a) $(m, n) = (5, 58)$, (b) $(m, n) = (5, 78)$, (c) $(m, n) = (5, 98)$, and ((a′)–(c′)) the corresponding far-field patterns obtained by using stationary phase method.

VCSELs have been investigated via controlling device temperatures [7]. It was confirmed that the near-field patterns of these high-order modes display the wavefunctions of equilateral triangular quantum billiards [7, 21]. Therefore, it is useful and pedagogical to elucidate the influence of the non-paraxial contribution to the high-order far-field pattern of VCSELs with optical apertures having an equilateral triangle shape.

For an equilateral triangular billiard with the vertices at $(0, 0)$, $(a/2, \sqrt{3}a/2)$, and $(-a/2, \sqrt{3}a/2)$, the quantum eigenstates $\Phi^{\pm}_{m,n}(x, y)$ are given by [21]

$$\Phi^{\pm}_{m,n}(x, y) = \sqrt{\frac{16}{a^2 3\sqrt{3}}}\left\{ e^{\pm i(m+n)(2\pi/3a)x} \sin\left[(m-n)\frac{2\pi}{\sqrt{3}a}y\right] + e^{\mp i(2m-n)(2\pi/3a)x} \sin\left[n\frac{2\pi}{\sqrt{3}a}y\right] - e^{\mp i(2n-m)(2\pi/3a)x} \sin\left[m\frac{2\pi}{\sqrt{3}a}y\right]\right\} \quad (11)$$

with $2n \geqslant m$ $(m = 1, 2, 3, \ldots; n = 1, 2, 3, \ldots)$, where m and n represent the order of the eigenstates and a is the side length of the equilateral triangle. Equation (11) is the representation of the traveling-wave eigenstates. The standing-wave representation of the eigenstates can be given by $S^{\pm}_{m,n}(x, y) = \Phi^{+}_{m,n}(x, y) \pm \Phi^{-}_{m,n}(x, y)$. The wave patterns of the eigenstates are generally confirmed to display honeycomb patterns [7]. To explore the influence of the non-paraxial contribution, we used equations (2) and (7) to calculate the near-field and far-field patterns for the lasing modes $S^{\pm}_{m,n}(x, y)$ of VCSELs with different transverse orders. Figure 7 shows the numerical wave patterns $|S^{+}_{m,n}(x, y)|^2$ (figures 7(a)–(c)) and the corresponding far-field patterns (figures 7(a′)–(c′)) with the transverse order of $(m, n) = (5, 58)$, $(m, n) = (5, 78)$, and $(m, n) = (5, 98)$. As seen in figure 5 for the case of square billiards, the non-paraxial contribution causes the far-field patterns to display the feature of pincushion curving. To sum up, the characteristic of pincushion curving is a typical sign of a non-paraxial contribution to the far-field patterns.

5. Conclusion

In conclusion, we have experimentally investigated the difference between the low-order and high-order far-field transverse patterns of VCSELs with a square-shape aperture. It was experimentally found that the high-order far-field patterns displayed the feature of pincushion curving with respect to the Fourier transform of the near-field wavefunction. We have theoretically confirmed that the pincushion curving arises from the non-paraxial contribution. On the basis of the stationary phase method, we have developed a fast procedure for obtaining the Fourier transform of the near-field patterns from the experimental far-field patterns, for accurately visualizing the momentum-space wavefunction of 2D quantum billiards. Finally, we have also analyzed the influence of the non-paraxial contribution for equilateral triangular VCSELs to confirm that the pincushion curving of the far-field pattern is a typical feature in high-order transverse modes.

Acknowledgment

The authors thank the National Science Council for their financial support of this research under Contract No. NSC-97-2112-M-009-016-MY3.

References

[1] Chow W W, Choquette K D, Hagerot-Crowford M, Lear K L and Hadley G R 1997 *IEEE J. Quantum Electron.* **33** 1810–24
[2] Deppe D G, Huffaker D L, Oh T, Deng H and Deng Q 1997 *IEEE J. Sel. Top. Quantum Electron* 3 893–904

[3] Chang-Hasnain C J, Harbison J P, Hasnain G, Von Lehmen A C, Florez L T and Stoffel N G 1991 *IEEE J. Quantum Electron.* **27** 1402–9
[4] Cheng D L, Yen T C, Chang W, Kuo W C, Kao K S and Hsu C P 2007 *IEEE Photon. Technol. Lett.* **19** 1961–3
[5] Spencer P S, Mirasso C R, Volet P and Shore K A 1998 *IEEE J. Quantum Electron.* **34** 1673–9
[6] Hegarty S P, Huyet G, McInerney J G and Choquette K D 1999 *Phys. Rev. Lett.* **82** 1434–7
[7] Chen C C, Su K W, Chen Y F and Huang K F 2008 *Opt. Lett.* **33** 509–11
[8] Huang K F, Chen Y F, Lai H C and Lan Y P 2002 *Phys. Rev. Lett.* **89** 224102
[9] Chen C C, Liu C C, Su K W, Lu T H, Chen Y F and Huang K F 2007 *Phys. Rev.* E **75** 046202
[10] Gensty T, Becker K, Fischer I, Elsäßer W, Degen C, Debernardi P and Bava G P 2005 *Phys. Rev. Lett.* **94** 233901
[11] Berggren K F, Sadreev A F and Starikov A A 2002 *Phys. Rev.* E **66** 016218
[12] Zozoulenko I V, Schuster R, Berggren K F and Ensslin K 1997 *Phys. Rev.* B **55** R10209
[13] Zozoulenko I V and Berggren K F 1997 *Phys. Rev.* B **56** 6931
[14] Chen C C, Yu Y T, Chen R C C, Huang Y J, Su K W, Chen Y F and Huang K F 2009 *Phys. Rev. Lett.* **102** 044101
[15] Carter W H 1972 *J. Opt. Soc. Am.* **62** 1195–201
[16] Chen Y F, Huang K F and Lan Y P 2002 *Phys. Rev.* E **66** 046215
[17] Haus H A 1984 *Waves and Fields in Optoelectronics* (Englewood Cliffs, NJ: Prentice-Hall)
[18] Zhou G 2010 *J. Opt. Soc. Am.* A **27** 890–4
[19] Mei Z and Zhao D 2008 *J. Opt. Soc. Am.* A **25** 537–42
[20] Duan K and Lü B 2003 *Opt. Express* **11** 1474–80
[21] Chen Y F and Huang K F 2003 *Phys. Rev.* E **68** 066207